Published in final edited form as:

Int J Hyperthermia. 2016 August ; 32(5): 543–557. doi:10.3109/02656736.2016.1159737.

Image-guided thermal therapy with a dual-contrast magnetic nanoparticle formulation: A feasibility study

Anilchandra Attaluri[a,*], **Madhav Seshadri**[a,*], **Sahar Mirpour**[b], **Michele Wabler**[a], **Thomas Marinho**[a], **Muhammad Furqan**[a], **Haoming Zhou**[a], **Silvia De Paoli**[c], **Cordula Gruettner**[d], **Wesley Gilson**[e], **Theodore DeWeese**[a], **Monica Garcia**[a,f], **Robert Ivkov**[a,g,h,i,†], and **Eleni Liapi**[b,†]

[a]Department of Radiation Oncology and Molecular Radiation Sciences, Johns Hopkins University School of Medicine, Baltimore, Maryland [b]Department of Radiology and Radiological Sciences, Johns Hopkins Hospital, Baltimore, Maryland [c]Center for Biological Evaluation and Research, Food and Drug Administration, Bethesda, Maryland, USA [d]Micromod Partikeltechnologie, GmbH, Rostock, Germany [e]Siemens Healthcare Solutions, Inc., Baltimore, Maryland, USA [f]Department of Genetics and Morphology, Institute of Biological Sciences, University of Brasilia, Brazil [g]Department of Oncology, Johns Hopkins University School of Medicine, Baltimore, Maryland [h]Institute for NanoBioTechnology, Johns Hopkins University, Baltimore, Maryland [i]Department of Materials Science and Engineering, Johns Hopkins University, Baltimore, Maryland, USA

Abstract

Purpose/objective—The aim of this study was to develop and investigate the properties of a magnetic iron oxide nanoparticle–ethiodised oil formulation for image-guided thermal therapy of liver cancer.

Materials and methods—The formulation comprises bionised nano-ferrite (BNF) nanoparticles suspended in ethiodised oil, emulsified with polysorbate 20 (BNF-lip). Nanoparticle size was measured via photon correlation spectroscopy and transmission electron microscopy. *In vivo* thermal therapy capability was tested in two groups of male Foxn1^{nu} mice bearing subcutaneous HepG2 xenograft tumours. Group I (n =12) was used to screen conditions for group II (n =48). In group II, mice received one of BNF-lip (n =18), BNF alone (n =16), or PBS (n =14), followed by alternating magnetic field (AMF) hyperthermia, with either varied duration (15 or 20 min) or amplitude (0, 16, 20, or 24 kA/m). Image-guided fluoroscopic intra-arterial injection of

CONTACT: Robert Ivkov, rivkov1@jhmi.edu, David H. Koch, Cancer Research Building, Rm 442, Department of Radiation Oncology and Molecular Radiation Sciences, Johns Hopkins University School of Medicine, 1550 Orleans Street, Baltimore, MD 21231, USA.

*Authors R.I and E.L. contributed equally to the paper.

†A.A. is now at the Department of Mechanical Engineering, Rowan University, Glassboro, NJ, USA. A.A. contributed equally to heating rate measurements, mouse experiments, AMF hyperthermia, data analysis, and manuscript preparation; M.S. contributed equally to mouse and cell culture experiments.

Disclosure statement

C.G. is an employee of micromod Partikeltechnologie, GmbH, manufacturer of the BNF nanoparticles used in this study. R.I. and E.L. are inventors of nanoparticle patents. All patents are assigned to either the Johns Hopkins University or Aduro Biosciences, Inc. All other authors report no conflicts of interest. This work was funded by the National Cancer Institute (grant numbers U54CA151838, P50CA062924, R21CA161626, 5R01CA194574-02 and P30CA006973). The authors alone are responsible for the content and writing of the paper.

BNF-lip was tested in New Zealand white rabbits (n =10), bearing liver VX2 tumours. The animals were subsequently imaged with CT and 3 T MRI, up to 7 days post-injection. The tumours were histopathologically evaluated for distribution of BNF-lip.

Results—The BNF showed larger aggregate diameters when suspended in BNF-lip, compared to clear solution. The BNF-lip formulation produced maximum tumour temperatures with AMF >20 kA/m and showed positive X-ray visibility and substantial shortening of T1 and T2 relaxation time, with sustained intratumoural retention up to 7 days post-injection. On pathology, intratumoural BNF-lip distribution correlated well with CT imaging of intratumoural BNF-lip distribution.

Conclusion—The BNF-lip formulation has favourable thermal and dual imaging capabilities for image-guided thermal therapy of liver cancer, suggesting further exploration for clinical applications.

Keywords

Computed tomography; embolisation therapy; hyperthermia; image-guided delivery; Lipiodol; magnetic nanoparticles; magnetic resonance imaging

Introduction

Image-guided therapies, aimed at palliative treatment of patients with unresectable primary or metastatic liver cancer include various intra-arterial and percutaneous ablative procedures, placing a heavy reliance on imaging for tumour targeting and response assessment [1]. Intra-arterial therapies, such as transcatheter arterial chemoembolisation (TACE), exploit the preferential hepatic arterial blood supply of liver tumours to selectively deliver high concentrations of drugs via the intra-arterial route, thus minimising systemic toxicity [1–8]. Despite significant advances during the past two decades, high rates of tumour recurrence and disease progression following treatment of locally advanced liver cancer remain unresolved issues, urging the need for development of novel approaches.

The effectiveness of hyperthermia as part of multi-modal therapy for cancer is well established, because its effects on tumour structure and physiology enhance drug perfusion, and its biological activity increases the therapeutic benefits of many drugs [9]. Yet technological barriers to implementation persist, inhibiting its widespread use and limiting its role in disease management [9]. Targeted hyperthermia achieved by remotely heating magnetic iron oxide nanoparticles (MIONs) via alternating magnetic fields (AMF) has emerged as a promising technology to treat a wide array of malignancies [10,11] and its use with image guidance was proposed shortly after the inception of TACE [12–16]. It was recognised early that MIONs conferred the additional potential to enhance therapeutic imaging with magnetic resonance (MR) following their delivery, and that this would aid treatment planning by providing an assessment of the tumour and overall hepatic iron distribution [17].

Despite the potential offered by ‘thermo-TACE’ with magnetic nanoparticles, its use for liver cancer disease management remains experimental and confined to animal models. Poor heating performance of nanoparticles and artefacts with MRI created by the high

concentrations of nanoparticles needed to overcome poor heating were identified in the early studies as significant barriers to clinical utility [17,18]. Conversely, advances in the synthesis of MIONs provide particles with significantly greater heating and drug delivery potential [18–22], and improved MRI techniques for imaging MIONs [23] motivate a renewed interest to develop image-guided delivery of magnetic nanoparticles for targeted hyperthermia.

Central to the development of nanoparticle constructs providing improved heating performance is the recognition that 1) superparamagnetism is neither a desired property for heating or imaging, nor is it necessary to ensure colloidal stability of the particles [24,25], and 2) that the magnetic anisotropy energy, the determinant of hysteresis loss power (i.e. heating), can be enhanced via collective magnetic interactions by aggregating magnetic nanocrystals [24–29]. Furthermore, it is now evident that these associations are complex, having an influence on multiple length scales, and that they are affected by interactions with an external magnetic field and immobilisation (when introduced into tissue) [24,28–32]. The magnetic nanoparticle constructs initially used for thermo-TACE comprised dextran-matrix nanoparticles containing dispersed iron oxide crystals having minimal collective magnetic associations within the particle, thereby limiting the realised magnetic anisotropy energy [18,25,27]. These were often combined with an ethiodised oil, such as Lipiodol®, or other carrier fluid used for TACE [2,18]. Ethiodised oil, a venerable and commonly used carrier fluid, was first synthesised in 1901 by Marcel Guerbet (1861–1938), a French pharmacist. Its preferential use for many image-guided procedures, including drug delivery derives from its radio-opacity (~48% iodine) and its ability to induce plastic and transient embolisation of tumour microcirculation [2,33–35]. Combining an ethiodised oil with nanoparticle constructs that rely upon an aggregated multi-crystallite core for heating has the potential to disperse the nanoparticle core and thus to disrupt the collective associations, thereby changing or reducing nanoparticle heating and imaging properties.

In this feasibility study we sought to determine whether a magnetic nanoparticle formulation comprising multi-crystallite core magnetic iron oxide nanoparticles and ethiodised oil might provide sufficient heating with AMF and image-guidance for transcatheter intra-arterial and intratumoural delivery in animal models. A commercial starch-coated iron oxide nanoparticle suspension was successfully combined with ethiodised oil to yield an emulsion (with ~1% polysorbate) that was stable for several days. Transmission electron microscopy and photon-correlation spectroscopy show that the ethiodised oil-emulsified particles have an increased size, suggesting a preferred clustering of a few particles. Heating measurements comparing particle-only with ethiodised oil-particle heating performance demonstrate that for a similar mass of iron, the ethiodised oil-particle emulsion heats more efficiently. This trend was consistent with *in vivo* heating measurements obtained in treated HepG2 human HCC xenograft tumours in mice. Preliminary studies on New Zealand white VX2 liver tumour-bearing rabbits demonstrate that the formulation can be injected via intra-arterial catheter in proximity to a liver tumour with positive X-ray properties during fluoroscopy, providing immediate feedback of successful tumour targeting. Positive X-ray properties of the formulation and intratumoural retention were subsequently confirmed and monitored with unenhanced X-ray computed tomography (CT) scans of the liver. MR imaging properties of the formulation revealed significant shortening of T1 and T2 relaxation time. Taken together, the results encourage further exploration of these novel higher-heating

'clustered' nanoparticle constructs for improving local tumour control with (dual) image guidance for therapy and follow-up.

Materials and methods

Magnetic iron oxide nanoparticles

The MIONs used for this study are commercially available aqueous suspensions of starch-coated magnetite (Fe_3O_4) core–shell bionised nanoferrite (BNF) particles (micromod Partikeltechnologie, Rostock, Germany). Synthesis and physical characterisation of the BNF particles is extensively documented [21,26–29,31,36]. Briefly, BNF particles are produced by precipitating ferric and ferrous sulphate salts from solution at high pH in a high-pressure homogenisation reaction vessel [21], which controls both crystal formation and aggregation to yield particles having high uniaxial anisotropy, measured by vector magnetometry in a saturating field to be $186.1 \pm 0.9 \times 10^{-7}$ N m at a concentration of ≈25 mg particles/mL [31]. As received from the manufacturer, they have a mean hydrodynamic diameter of ~120 nm and an iron content >70% w/w, with a total iron concentration of about 30 mg Fe/mL (42 mg particle/mL). Their heating properties when exposed to AMF and biocompatibility have been previously described [31,36].

Preparation of BNF and ethiodised oil emulsion

The MION emulsion, BNF-lip, used in this study, consists of a water-in-oil emulsion of aqueous BNF nanoparticles, suspended in ethiodised oil (Lipiodol Ultra-Fluide, Guerbet, Bloomington, IN), and emulsified with polysorbate-20 (Tween® −20, Sigma Aldrich, St Louis, MO). The ethiodised oil used in the present studies was Lipiodol, containing 48% iodine weight/volume or 480 mg iodine/mL. BNF-lip emulsion was prepared by adding 1% polysorbate-20 to BNF particle suspension, followed by 1 min vortexing. The ethiodised oil with 1% polysorbate-20 was then added to the BNF-polysorbate-20 mixture 1:1 v/v with mixing to yield BNF-lip emulsion. Fresh batches of BNF-lip were prepared before each experiment described below.

For photon correlation spectroscopy (PCS) and transmission electron microscopy (TEM) particle size measurements, a surrogate highly concentrated BNF-lip (cBNF-lip) emulsion was used. The cBNF-lip was prepared by combining BNF with polysorbate-20 as above. Following mixing, a BNF-rich fraction was collected using magnetic-assisted settling with a rare-earth permanent magnet for 20 min and decanting the supernatant. The particles were re-suspended with ethiodised oil and sonication (Sonorex Super 10P, Bandelin, Berlin, Germany) at a power of 320 W and frequency of 35 KHz for 30 min. Finally the suspension was filtered through a Millex-AP pre-filter (Millipore, Billerica, MA) to yield a paste of concentrated BNF emulsion for use in further characterisation. This step was necessary because the water-in-oil dispersion proved intractable for either characterisation technique. Moreover, the non-volatile ethiodised oil prevented drying on sample grids for TEM, and scattering from droplets in the emulsion precluded reliable and reproducible measurements of particle size with PCS.

Physical characterisation of BNF and BNF-lip

Nanoparticle size characterisation with transmission electron microscopy—

TEM was used to characterise BNF size(s) and potential changes of BNF aggregation when combined with ethiodised oil in cBNF-lip. TEM was performed on BNF particles and cBNF-lip using an EM 912 microscope (Zeiss, Oberkochen, Germany) working at 100 keV. Samples were diluted and spin-coated onto a carbon film-coated grid to isolate individual particles for imaging.

Nanoparticle size characterisation with photon correlation spectroscopy—

Size measurements were performed on samples by PCS with a Malvern Zetasizer Nano ZS-90 (Malvern Instruments, Malvern, UK). PCS was used to determine the hydrodynamic particle diameter of the samples. For BNF, samples were diluted in sterile water to an iron concentration of approximately 0.4 mg/mL prior to analysis. cBNF-lip samples were diluted to approximately the same concentration with ethanol. The refractive index of ethanol was used as an input parameter for analysis. The z-average size was used to estimate mean value for the nanoparticle hydrodynamic diameter.

In vitro measurement of iron content

Iron concentrations were determined with the Spectroquant-Kit (Merck, Darmstadt, Germany) using methods previously described [31]. Briefly three aliquots of either BNF particles, or formulation were weighed (5–10 mg) and digested with 200 μL concentrated hydrochloric acid at 70 °C for 10 min. Iron concentration was determined by spectroscopy following manufacturer recommendations.

In vitro specific heating rate measurements

The heating properties of ethiodised oil, BNF, and BNF-lip were measured with the vertical solenoid configuration and other equipment and methods described below (in AMF methods). Briefly, 1-mL volumes of sample (ethiodised oil, BNF, BNF-lip) or PBS were placed in standard 12-mm (5-mL) polystyrene test tubes and inserted into the AMF calorimeter [37]. Rate of rise of temperature for both BNF and BNF-lip suspensions were measured and compared by measurements of samples having Fe concentration fixed to 15 mg/ml. Samples were tested with varying AMF peak amplitude 0, 12, 14, 16, 20, 28, and 32 kA/m at frequency of 155 ± 5 kHz. Direct comparisons of heating between BNF and BNF-lip were performed at 20 and 32 kA/m. At each power setting a sample of ethiodised oil/distilled water/polysorbate-20, having proportions equal to those used in the nanoparticle emulsion was measured and subtracted to remove contributions from solvent(s) and calorimeter components. The heating ability of the particles is reported as specific heating rate, or (dT/dt) × (1/mg Fe), where dT/dt is the slope of temperature versus time curve and sample volume is assumed constant. For all measurements, sample volume was fixed at 1 mL. Procedures to estimate dT/dt have been previously reported [36]. Briefly, a constant volume of 1 mL suspension was placed in a standard 12 mm polystyrene test tube and inserted into the insulating sample holder. A fibre-optic temperature probe (FISO, Quebec, Canada) was immersed into the sample suspension. AMF power was applied after a stable temperature was established. At each power setting the temperature of a ‘blank’ i.e., water or a mixture of water and ethiodised oil without nanoparticles was also measured, and

subtracted from sample temperatures. The appropriate interval for calculating the slope of T versus t curve was determined by analysing a plot of the incremental temperature change, analogous to the first derivative of the heating rate as previously described [36].

Alternating magnetic field system

All nanoparticle heating experiments were conducted by exposure to alternating magnetic fields (AMFs) using equipment and methods as previously described [36,37–41]. These are summarised briefly to provide context for discussion. The AMF system comprises three main components: 1) the power source, 2) an external impedance matching (capacitance) network, and 3) the load which is a modified solenoid inductor having either vertical configuration for nanoparticle heating characterisation [36,37]; or, horizontal configuration with water-jacketed thermal regulation for mouse experiments [39,41]. The power source, matching network, and closed-loop circulating water/water cooling system (200-L reservoir of distilled water) are the same components for both solenoids and for all AMF experiments.

The power supply was an 80-kW induction heating system manufactured by PPECO (Watsonville, CA) providing alternating current with variable frequency between 135 kHz and 440 kHz, which was adjusted for stable oscillation at 155 ± 5 kHz using capacitors, as previously described [37,39]. Field amplitude measurements were conducted with commercially available field probes (AMF Life Systems, Auburn Hills, MI) and solenoid calibrations were performed with copper wire [38].

A water jacket, constructed from concentric polyacrylic tubing that was filled with distilled water, was placed inside the load [37]. The water jacket was designed to provide thermal control, set to 35.0° ± 0.5 °C, in the sample chamber with a closed-loop bench-top circulating bath (Hoefer Scientific Instruments, San Francisco, CA) capable of circulating water at 4 L/min. Additionally, the water jacket may provide thermal regulation for anaesthetised mice that commonly lose thermo-regulatory control and become hypothermic. Further, operation of the coil with its cooling system can add either heat sink or additional heat source to hyperthermia experiments with mice that depends upon the power setting used [39,41]. Stabilising the temperature of the sample environment for mouse hyperthermia experiments facilitates data interpretation [41].

Invasive thermometry

Temperatures were measured with RF-resistant fibre-optic temperature probes (FISO, Quebec, Canada). Temperatures were recorded at 1-s intervals, beginning after samples, i.e. nanoparticles or mice, were in place for a period of time before AMF exposure. For mouse experiments, time before AMF power was initiated was about 30 s, and for nanoparticle characterisation it varied depending upon measured temperature between sample and calorimeter. For nanoparticle characterisation experiments the nanoparticle sample and calorimeter were secured in the coil and allowed to thermally equilibrate (defined as temperature variation ≤ ± 0.2 °C in 30 s) at approximately 21.0 ± 0.6 °C. The AMF power was applied 30 s after the established criterion for thermal equilibration was met, and remained on for 60 s or until a temperature increase of 30 °C was measured [36–40].

Biological characterisation of BNF-lip formulation

Biological characterisation of nanoparticle-mediated heating with BNF particles alone has been previously documented [31,40,41]. The intent of the *in vivo* experiments in this study was to characterise the heating properties of the BNF-lip formulation in HepG2 xenograft tumours in Foxn1^{nu} mice, and to assess initial feasibility of image-guided transcatheter delivery and imaging abilities in the orthotopic rabbit liver VX2 tumour model using New Zealand white rabbits.

Sixty male nude mice (Hsd: Athymic Nude-Foxn1^{nu}, Harlan Labs, Indianapolis, IN) were used in this study. All were 4–6 weeks old and weighed 17–25 g prior to treatment. Ten male white New Zealand rabbits, weighing 4.0–4.5 kg were used in this study. The mice and rabbits were housed in an Association for Assessment and Accreditation of Laboratory Animal Care (AAALAC)-accredited facility in compliance with the *Guide for the care and use of laboratory animals* [42]. All procedures were approved by the Johns Hopkins Institutional Animal Care and Use Committee (IACUC). Male nude mice were selected for their relevance to other studies for cancer therapy. Rabbit species and gender were selected because of their relevance to model intra-arterial delivery of agents into liver tumours [43].

Thermal therapy in mice

All mice received a subcutaneous injection of 3×10^6 HepG2 cells (suspended in 0.1 mL PBS) in the thigh and were randomly assigned into one of several cohorts described below. Tumour volumes were calculated from caliper measurements of tumour dimensions in three orthogonal directions using a formula for a hemi-ellipsoid. Measurements were performed at regular intervals (2–4 days) once the tumour was palpable, usually 2–3 weeks after injection. When the calculated tumour volume was between ~0.1 cm^3 and ~0.25 cm^3 the mice received intratumoural injections of one of either a) PBS with 1% polysorbate 20, b) BNF +PBS 1:1 v/v + 1% polysorbate 20, or c) BNF-lip depending upon individual cohort assignment. The dose was determined as $Dose\ (D) = V_{inject}/V_{tumour}$ where V_{inject} and V_{tumour} are volumes of injected material and tumour, respectively in units of cm^3. Intratumoural injections were performed manually with 26-gauge needles. Rate of injection varied, roughly 0.02 mL/s. Volumes of injected material in each mouse are provided in Table 1. BNF concentration in the nanoparticle-containing materials was ~15 mg Fe/mL (~21 mg particle/mL).

A preliminary series of magnetic hyperthermia experiments was conducted in a group of 12 mice (group I), which received either variable dose of BNF-lip (constant AMF amplitude) or variable AMF amplitude (constant BNF-lip dose). Three AMF amplitudes (14, 16, or 20 kA/m) and four injection doses (D =0.25, 0.5, 0.75, 1.0 = V_{tumour} (mL)) were tested to identify optimal heating and BNF-lip conditions.

A second series of hyperthermia experiments was conducted with a larger cohort, group II, of 48 tumour-bearing mice for which D was fixed at 0.5 V_{tumour} (mL) and mice were randomly assigned into one of three groups: 1) BNF-lip (18), 2) BNF (16), or 3) PBS (14). Cohorts were further subdivided for hyperthermia with amplitude of 0 (3), 16 (4), 20 (40), or 24 (1) kA/m and duration of either 15 (18) or 20 (30) min. Conditions used in this series of experiments and results of thermometry are summarised in Table 1.

The animals were anaesthetised 18 h after the BNF-lip injection and were treated with AMF using the horizontal inductor configuration and water jacket (setting of 35 °C) as described above. For each mouse, three temperature probes were used, placed in the tumour centre, the rectum, and on the abdominal skin surface.

Rabbit liver VX2 tumour implantation procedure

VX2 tumour sections were implanted in the livers of 10 New Zealand white rabbits for eventual intra-arterial injection with BNF-lip for assessing feasibility of intra-arterial delivery and subsequent dual (MRI and X-ray) imaging of model liver tumours. Each pre-anaesthetised rabbit was placed in a supine position, shaved in the subxyphoid area, and prepped in a sterile fashion following methods previously described [43,44]. Using real-time ultrasound (US) guidance (7.5-MHz linear transducer, Aloka, Wallingford, CT), percutaneous implantation of two aliquots (0.1 mlL) of VX2 tumour pieces (previously excised from the thigh of a rabbit VX2 tumour carrier) was performed via a 21-gauge angiographic catheter. After implantation, the angiographic catheter was removed and light manual compression was performed on the site of tumour inoculation for 2 min. The tumour was then allowed to grow for 11–17 days, at which time the tumour longest axial diameter ranged between 1.0 and 2.5 cm, and the animals were subsequently intra-arterially injected with BNF-lip or PBS (control).

Image-guided intra-arterial injection in rabbits

Intra-arterial image-guided delivery of BNF-lip or control saline to VX2 tumour-bearing rabbits was performed following previously described methods [45,46]. Rabbits were pre-anaesthetised and anaesthetised with inhalant isoflurane (1.5–5% in oxygen). Angiographic studies were performed via a surgical cut-down of the femoral artery and insertion of a 3 Fr vascular sheath (Performer^{TM} Introducer, Cook Medical, Bloomington, IN). A 2 Fr J1 polyethylene angiographic catheter (Cook Medical, Bloomington, IN) was subsequently advanced to the coeliac axis and a diagnostic angiography was performed for the delineation of the common, right, and left hepatic arteries, secondary/tertiary branches of the hepatic artery, as well as the tumour-feeding artery. After identifying the tumour blush and confirming proper catheter positioning, a volume equal to 0.5 of measured tumour volume (~0.5 mL) of BNF-lip or PBS was injected. Fluoroscopic guidance was used to identify appropriate tumour targeting. A post-injection single-shot X-ray was performed to document BNF-lip tumour targeting.

CT imaging protocol

All VX2 tumour-bearing rabbits were imaged in a clinical wide-detector X-ray CT scanner (Acquilion ONE, Toshiba, Tokyo, Japan) with and without contrast medium, at baseline, 48 h (4) or 7 days (6) post-intra-arterial injection. CT scanning of the liver was performed to determine whether imaging of intratumoural distribution of injected BNF-lip was feasible. For imaging the liver and tumour with CT, the following parameters were used: 120 kV tube voltage; 80 mA tube current; 0.5 s gantry revolution time; 1 mm pixel spacing; 512 × 512 pixel (spatial resolution); and 0.5 mm reconstructed slice thickness. First, an unenhanced scan was performed. Second, dynamic CT scanning was initiated with a scan delay time of 6 s following injection of contrast agent. For intravenous contrast medium injection, a 21-

gauge butterfly needle was inserted into a rabbit auricular vein. Injection of 7 mL (1.5 mL/kg body weight at 1 mL/s) iso-osmolar contrast agent (Visipaque™ 320, GE Healthcare, Wauwatosa, WI) was followed by saline flush (5 mL at 1 mL/s). The injection of contrast medium facilitated delineation of tumour vascularity.

CT data analysis

CT images were post-processed using two dedicated imaging software tools. First, images were transferred to the adjacent Toshiba workstation equipped with dedicated software (Body Registration and Body Perfusion, Toshiba Medical Systems) for motion correction in all three planes and subsequent image registration. Images were then transferred to a freely downloadable open source image analysis software package, OsiriX® (version 5.9, 32-bit, www.osirix-viewer.com). BNF-lip conspicuity was assessed qualitatively and quantitatively on axial pre-contrast CT scans of the liver by two radiologists in consensus. Qualitative assessment included targeted BNF-lip localisation in the tumour defined as either absent or present. When it was determined to be present, intratumoural BNF-lip distribution was assessed according to intensity as mild, moderate or high, and according to location as central, peripheral at the tumour rim, or covering the majority of tumour volume. Non-targeted BNF-lip localisation was also assessed as present or absent. Quantitative assessment of BNF-lip distribution after intra-arterial injection included the application of circular regions of interest (ROI) on axial unenhanced images at the tumour at its axial longest diameter and surrounding hepatic parenchyma. For each ROI, the maximum, minimum, and mean Hounsfield units (HU) were recorded.

MRI imaging protocol

Livers of rabbits imaged with CT were also imaged in a clinical MR scanner (3 T, Magnetom Trio, Siemens Healthcare, Malvern, PA) with and without contrast medium, at baseline, 48 h (4), or 7 days (6) post-intra-arterial injection. MR imaging of the liver was performed to assess intratumoural distribution of injected BNF-lip. Each animal was placed inside an 8-channel knee coil, covered with a blanket and allowed to breathe freely. The imaging protocol consisted of transverse T2-weighted turbo-spin echo images (matrix size 256 × 154, slice thickness 2 mm, interslice gap 2.2 mm, repetition times 8110 ms, echo times 99 ms, flip angle 158°, slice thickness 2 mm, interslice gap 2.2 mm), transverse T2*-weighted 2D gradient echo (GRE) images (matrix size 256 × 186, repetition times 200 ms, echo times 2.34–25.1 ms, flip angle 20°, slice thickness 2 mm, interslice gap 3 mm) for generation of R2*-weighted imaging maps at the tumour level, transverse T1-weighted 2D dual echo in-phase and out-of-phase spoiled gradient recall echo images (matrix 256 × 192, repetition times 166 ms, echo times 4.9 ms for the in-phase and 2.46 ms for the out-of-phase images, flip angle 70°, slice thickness 3 mm, interslice gap 3 mm) and T1-weighted three-dimensional volumetric interpolated breath-hold examination (VIBE) fat-suppressed spoiled gradient-echo images (matrix 256 × 154, slice thickness 2 mm, repetition times 4.33 ms, echo times 4.33/1.44 ms, flip angle 13), before and after injection of 0.3 mmol/kg gadobutrol (Gadavist, Bayer Healthcare, Whippany, NJ).

MRI data analysis

MR images were transferred to the OsiriX® freeware platform for quantitative analysis of signal intensity (SI) values on the GRE, as well as the in- and out-of phase sequences. Representative regions of interest (ROI) were drawn at one location of each liver lobe and one tumour location, covering the entire tumour axially and at the slice of the longest unidimensional axial tumour diameter. All ROIs were placed at least 1 cm from the external liver capsule, in order to minimise the effect of signal alteration from adjacent structures or susceptibility artefact from surrounding air or in the lungs. GRE values were recorded based on the average numerical value within each ROI. The same ROIs were subsequently copied into the in-phase and out-of phase sequences and all images were viewed in parallel synchronisation, for ROI SI value measurements.

Histopathology evaluation

Histopathological evaluation of HepG2 tumour in mice, liver and VX2 tumours in rabbits was performed as follows. After AMF hyperthermia, mice were euthanised either at 24 h (15) or 3 days (3) after treatment for histopathological assessment of tumour necrosis and intratumoural iron deposition. Rabbits were euthanised 7 days after intra-arterial injection with BNF-lip and liver and VX2 tumours were harvested. Excised tumours were fixed in 10% formalin and routinely processed and embedded in paraffin. Sections were cut and stained with haematoxylin and eosin (H&E) and Prussian blue (PB) stain. For tumour necrosis quantification, images were acquired at 2 × magnification and analysis was carried out using the open-source ImageJ software (http://rsb.info.nih.gov/ij/). The dynamic range of images was expanded to full by contrast enhancement, and necrotic and total tissue areas were recognised using different filter values under direct human supervision. Black areas in the final binary images were quantified in terms of pixel counts to obtain a percentage necrotic index expressed as (necrotic area)/(total tissue area) × 100.

For the qualitative assessment of iron deposition, PB-stained slides of tumour and liver tissues were evaluated at 5×, 10× and 40× magnification for identifying the pattern of iron distribution in tumour and liver tissue (central, peripheral, or dispersed), the PB stain intensity (none, minimal, moderate, mild or marked), the presence of iron in vascular areas, as well as the presence of iron in endothelial cells, hepatocytes, or Kupffer cells.

Statistical analysis

Statistical analysis was performed using STATA software (STATA version 12, StataCorp, College Station, TX). Numerical data were expressed as means ± SD. Paired two-sample t-tests and chi-square tests were performed and a *P*-value of <0.05 was considered to indicate statistical significance.

Results

Physical characterisation of BNF and BNF-lip

Nanoparticle size characterisation with PCS and TEM—TEM images of BNF nanoparticles (Figure 1(A)) show that individual particle cores are comprised of multiple iron oxide crystals aggregated into elongated fractal patterns with long axis dimension <200

nm. This is consistent with previous observations, and is considered responsible for the measured high uniaxial anisotropy [25,28,31,36]. When combined with ethiodised oil, as in cBNF-lip, nanoparticle clustering is modified to reveal multiple large spherical clusters of iron oxide surrounded by lower intensity regions, suggesting an ethiodised oil 'coating' (Figure 1(B)). The central dense clusters have diameter of ~250 nm, consistent with PCS data obtained (Figure 1(C)). In addition, filaments of ethiodised oil extend from the central mass and contain high-intensity punctate foci, suggesting individual (or small clusters of) iron oxide crystals have separated from cores of individual particles that are stabilised with an ethiodised oil coating (Figure 1(B)). The size of the entire object appears to be >1 μm.

Mean particle diameter measured with PCS was 120 nm for BNF solution and mean aggregate diameter was 276 nm for the cBNF-lip (Figure 1(C)), generally consistent with TEM images. Interestingly, the larger aggregates (> 1 μm) observed in TEM do not appear in PCS, presumably because the low-density filamentous portions were dispersed in the solvent (ethanol).

In vitro specific heating rate measurements—The time–temperature data obtained from both BNF and BNF-lip using two AMF settings having peak amplitudes of 20 and 32 kA/m are shown in Figure 2(A). Heating rates of BNF-lip are slightly but consistently higher than for BNF alone. The measured specific heating rate of BNF-lip was higher (>30%) than BNF alone, that is, 0.08 °C/(s × mg Fe), compared with 0.06 °C/(s × mg Fe) when subjected to an AMF amplitude of 20 kA/m and 155 ± 5 kHz. Interestingly, the comparative difference in specific heating rate between BNF-lip and BNF reduced to 11%, although BNF-lip still displayed higher heating rate, at the higher amplitude of 32 kA/m.

Amplitude-dependent heating of the BNF-lip is reported in Figure 2(B). Significant heating rate increases occur between 14 and 16 kA/m, and again at 20 and 28 kA/m suggesting significant heating properties at the higher peak amplitudes. Ethiodised oil does not contribute to heating at this frequency (data not shown), and the high-amplitude heating performance is consistent with BNF particle heating in suspension [36].

Biological characterisation of BNF-lip formulation

AMF hyperthermia in mice—AMF hyperthermia treatments were well tolerated by all mice. The measured temperature change of tumours for group I mice are shown in Figure 3(A). Higher measured tumour temperatures generally correlated with increased volume of injected BNF-lip and at higher AMF amplitude. Significant leakage, however, occurred with consistently injecting BNF-lip (and other sample fluids) at a dose of $D = 1.0\ V_{tumour}$ (mL), thus injected volume for group II was fixed at $0.5\ V_{tumour}$.

For group II mice, a summary of experimental conditions and measured initial and final temperatures (tumour and rectal) are provided in Table 1. Mean temperature data measured for 15-min and 20-min treatments are displayed in Figures 3(B) and 3(D), respectively. Figures 3(C) and 3(E) display mean differences between measured tumour and rectal temperatures for all cohorts within group II.

Image-guided intra-arterial injection in rabbits

Image-guided intra-arterial BNF-lip injection was feasible and successful in all rabbits. BNF-lip was easily and successfully injected via a 2-Fr catheter and was visualised with positive X-ray properties during angiographies. Confirmation of BNF-lip intratumoural deposition was feasible in all animals, with standard single-shot abdominal X-rays (Figure 4(A)). A representative pre-injection MRI image of rabbit liver and tumour is shown in Figure 4(B). Figures 4(C) and 4(D) show representative post-injection MR and X-ray CT image slices of tumour containing BNF-lip. Interestingly, the angiographic intratumoural distribution of BNF-lip had a distribution pattern resembling that of intra-arterially ethiodised oil, primarily along the tumour vessels of the tumour periphery (Figures 4(A) and 4(D)) [45–47].

CT data analysis

BNF-lip was successfully identified as high attenuation, positive X-ray contrast material within the tumour in all injected rabbits. BNF-lip was determined to be distributed dispersedly within tumours in 7/10 rabbits and only at the tumour edge in 3/10 rabbits. Intratumoural BNF-lip CT attenuation was graded as intense in 7/10 rabbits and mild in 3/10 rabbits. In tumours displaying high contrast (intense HU attenuation), BNF-lip was observed to involve the majority of the tumour volume. Most animals imaged at 48 h (3/4) had well-targeted tumours, whereas slightly fewer rabbits imaged at 7 days (4/ 6) showed intense intratumoural attenuation of BNF-lip.

Well-targeted tumours displayed a statistically significant attenuation in tumour ROI (mean 202.44 HU, SD 73.68 HU) than did partially targeted tumours (mean 91.90 HU, SD 16.92 HU, p =0.03). Well-targeted and partially targeted tumours, however, had similar minimum HU attenuation values (well-targeted mean 17.57, SD 13.15 HU; partially targeted mean 20, SD 1 HU, p =0.76) and similar maximum HU values (well-targeted mean 884, SD 529.30 HU; partially targeted mean 354, SD 297.14 HU, p =0.14). Mean liver ROI HU attenuation values were similar lying between well-targeted and partially targeted tumours (well-targeted tumours mean liver ROI density 79.64 HU, SD 17.78; partially targeted-tumours mean liver ROI density 86.52, SD 10.12, p =0.55). Interestingly, the minimum liver HU values of well-targeted tumours were lower than the minimum HU values of partially targeted (well-targeted minimum liver HU ROI mean 40.85, SD 8.02; partially targeted mean 55, SD 10.81 HU, p =0.04), suggesting that the off-target BNF-lip material remained within the surrounding liver parenchyma of partially targeted tumours and for up to 7 days.

MR data analysis

BNF-lip was successfully identified as dispersed, very low intensity material within tumours and liver in all treated rabbits. The qualitative evaluation of BNF-lip distribution revealed that tumours were successfully targeted with BNF-lip; however, specific patterns of distribution could not be identified, as with CT imaging, due to the pronounced magnetic features of iron, and consequent susceptibility artefacts (see Figure 4(D) for representative MR slice).

There was a statistically significant reduction in SI of tumour and liver ROIs after injection of BNF-lip, in all T1-weighted sequences, attributed to the presence of iron oxide nanoparticles throughout the tumours and liver. Mean tumour ROI SI in the in-phase (TE 4.91 ms) sequence was 407.42 (SD 97.03) before injection and was reduced to 177.88 (SD 100.66, p <0.0001), corresponding to an average 56% reduction in signal intensity after injection. Similarly, mean liver ROI SIs in the in-phase sequence were lower after injection for either hepatic lobe (left liver pre-injection mean 473.06, SD 177.74, post-injection mean 205.51, SD 122.36, p <0.0001; right liver pre-injection mean 475.46, SD 117.16, post-injection mean 201.97, SD 106.49, p <0.00001). Mean tumour ROI SI in the out-of-phase (TE 2.46 ms) sequence was 482.93 (SD 127.77) before injection and was reduced to 309.78 (SD 146.93) after injection (35% change, p =0.001). Similarly, mean liver ROI SI in the out-of-phase sequence were lower after injection for either hepatic lobe (left liver pre-injection mean 574.45, SD 140.15, post-injection mean 338.38, SD 171.81, p =0.0002; right liver pre-injection mean 593.47, SD 112.96, post-injection mean 404.75, SD 185.89, p =0.001).

Histopathology

Histological examination of H&E- and PB-stained tumour slides was carried out in all mice. In H&E-stained tumour slides of mice euthanised 24 h after AMF hyperthermia treatment, for tumours in heated and unheated BNF and BNF-lip groups, all groups showed small necrotic areas corresponding to the iron nanoparticle distribution as seen on and compared to relevant PB-stained tumour slides (mean area showing necrosis 12%, SD 5.11%). Figures 5(A) and 5(B) are representative images of an excised HepG2 tumour section from a mouse into which BNF-lip was injected, and 3 days after AMF hyperthermia. In the BNF group, iron nanoparticles aggregated in the centre of the tumour, as well as the vicinity of the presumed needle track. Similarly, in the BNF-lip group, iron nanoparticles aggregated in the centre of the tumour and presumed needle track, but also in the vascular spaces at the tumour rim. This is consistent with previous observations of ethiodised oil intratumoural transport properties [48,49].

Histological examination of H&E-stained rabbit tumour and liver slides revealed an average percentage area of tumour necrosis of 35.6% (SD 17.33%) 7 days after intra-arterial BNF-lip injection. BNF-lip on PB-stained tumour and liver slides displayed accumulation primarily at the tumour vascular rim and in endovascular spaces, as well as inside endothelial cells, hepatocytes and Kupffer cells (Figures 5(C) and 5(D)). Iron intensity on PB-stained slides was characterised as moderate and dispersed in 7/10 rabbits and moderate but confined to the rim in 3/10 rabbits, highly correlating with the CT pattern of BNF-lip.

Discussion

The aim of this feasibility study was to investigate the potential utility of a formulation containing ethiodised oil (ethiodised oil) and nanoparticles comprising aggregated iron oxide cores for hyperthermia and imaging of liver cancer. This effort was directed towards assessing the performance of a magnetic nanoparticle construct that derives significant heating advantage from collective magnetic interactions within an aggregated core of iron oxide crystals [21,24,25,28–31]. Iron oxide crystals are hydrophobic, and combining these

nanoparticles with lipid-based carrier fluids and surfactants has the potential to disperse the cores and significantly alter their heating properties. Ethiodised oil has been used for intra-arterial delivery and treatment of unresectable liver cancer [1,2,4–8]. In this study we exploited the properties of nanoparticles and ethiodised oil to selectively deliver the nanoparticles to the tumour and subsequently generate mild hyperthermia with the use of alternating magnetic fields.

The overall size of nanoparticles is a critical *physico*chemical property that affects their *physico*chemical properties for biological applications [50]. Furthermore, size of the magnetic portion (i.e. core) of the particles is a critical property that determines hysteresis heating for hyperthermia applications [24], yet measurements proved challenging for the formulation used in this study. The overall size of the particles with coating was measured by PCS, and iron oxide cores were estimated from TEM images. Attempts to measure particle size of BNF-lip suspensions were unsuccessful, necessitating a modification of the procedure to produce cBNF-lip formulation. This alteration limits interpretation from subsequent measurements with BNF-lip formulations; however, general consistency is tantalising and motivates future investigation. Estimates of nanoparticle size within the cBNF-lip formulation using both PCS and TEM (Figure 1(B) and 1(C)) suggest a redistribution of iron oxide crystals (or cores) during formulation generating consistently larger structures compared with the original BNF suspension (Figures 1(A) and 1(C)). Noteworthy is the fact that PCS may become less reliable for measuring size in samples containing wide particle size distributions because the scattered light intensity depends upon the sixth power of the size of the scattering object [51]. The observed narrowing of size distribution (cBNF-lip versus BNF) for the formulation as seen in PCS (Figure 1(C)) may thus be misleading because smaller dispersed crystal structures observed in TEM are not apparently represented in the PCS data. It is worth noting, however, that TEM provides no volumetric comparisons and thus a quantitative determination of particle size awaits additional measurements and analysis.

Measurements of heating performance with BNF-lip are generally consistent with the increased size of magnetic cores [24]. BNF nanoparticles demonstrate a significant non-linear dependence of increased heating rate with AMF amplitude [36] arising from both crystal aggregation and high uniaxial anisotropy [21,24,27–29,31,36]. This amplitude-dependence is generally preserved and seems to be enhanced in the BNF-lip (Figure 2(B)) indicating a preservation of anisotropy; whereas the increased heating (Figure 2(A)) is consistent with the particle sizing data. Specific heating rate data (Figure 2(A)) directly comparing BNF and BNF-lip formulations demonstrate increased heating of the formulation that decreases as magnetisation saturation is approached (> 32 kA/m). The high concentration of the cBNF-lip and its insolubility in water precluded heating rate testing for direct comparison with either BNF or BNF-lip. Despite this limitation, the observed trends in heating are consistent with measurements of generally increased size of iron oxide nanoparticle clusters.

The improved heating performance of the BNF-lip formulation translated to *in vivo* testing in mouse models of HCC tumours. Initially, a first group of mice (group I) was divided into 12 cohorts (1 per cohort) to screen injected volume and AMF amplitude parameters for

detailed exploration in a subsequent group of subjects (group II). Generally increased heating was found with both injected volume of BNF-lip and AMF amplitude (Figure 3(A)). On the other hand, inconsistent delivery of BNF-lip at the highest tested volume ($D = 1.0\,V_{tumour}$) provided guidance to fix the dose for group II mice at a value of $0.5\,V_{tumour}$.

Additional testing was conducted to further refine parameters for group II. A cohort of 18 mice was subjected to varying AMF amplitude with limited duration (15 min), after having received one of BNF, saline (PBS), or BNF-lip injections into their tumours. Study conditions are summarised in Table 1, and mean tumour surface temperature data are provided in Figure 3(B). Finally, a cohort of 30 mice was tested after receiving injections having volume fixed at $0.5\,V_{tumour}$, AMF amplitude fixed to 20 kA/m (except sham controls, i.e. 0 kA/m), and duration fixed to 20 min. As above, experimental parameters are summarised in Table 1, and mean tumour temperature data are reported in Figure 3(D). In all cases, increased tumour (Figures 3(B) and 3(D)) and rectal temperatures (Table 1) were recorded at greater AMF peak amplitudes; however, consistently higher tumour temperatures were achieved with BNF-lip and BNF than with saline controls. Furthermore, consistently higher tumour temperatures were recorded for BNF-lip than for BNF, suggesting that the observed *in silico* heating increase was preserved *in vivo*. In both Figures 3(B) and 3(D), the horizontal solid line illustrates the water jacket temperature setting of 35 °C.

In all cases the mean initial tumour temperature (T_0) measured for all cohorts of mice was below 35 °C at the start of AMF exposure (i.e. t = 0 s). Thus, some of the measured initial temperature rise is attributable to thermal adjustment of the mouse to the sample environment temperature. It is well established that exposing mice to AMF at ~150 kHz generates amplitude-dependent non-specific tissue heating that also increases with increased radius of exposed tissue [37,41,52,53]. Thus, temperature rise measured at the surface of a subcutaneous tumour is expected to always exceed rectal temperature rise until or unless cooling mechanisms become involved [39,41,52]. Active cooling with a water jacket thus provides a thermal-stabilising chamber that warms a hypothermic subject and provides cooling when hyperthermic temperatures are encountered [39,41]. The interplay between these two effects, with AMF heating is observed by comparing differences of tumour and rectal temperatures (i.e. $T_{tumour} - T_{rectal}$) for both saline and sham cohorts (Figures 3(C) and 3(E)). An initial rise in this difference suggests warming at the surface (i.e. tumour) followed by eventual cooling at the surface, evidenced by a decreasing temperature difference at time > ~150 s. These changes are subtle (≤ 0.5 °C) and suggest that amplitude-dependent non-specific heating is a negligible factor in these experiments, and that active temperature regulation in the sample environment is beneficial. Comparison of differences between tumour and rectal temperatures in the mice, particularly in PBS (saline) cohorts, provides a measure of the extent of non-specific heating, or temperature rise due to AMF interactions with tissue. For nanoparticle-containing mice (BNF and BNF-lip), however, this difference demonstrates significant heating from BNF particles that is demonstrably higher in BNF-lip cohorts (15 and 20 min; Figures 3(C) and 3(E)). Clearly, both BNF and BNF-lip lead to increased specific tumour heating, with the latter formulation providing the greatest heating potential.

To further assess the relative heating from non-specific AMF, BNF, or BNF-lip we calculated the difference between final and initial temperatures at the surface of the tumour or rectum (Table 1). Mean values obtained from the 20-min cohort of these are presented in Figure 6 for comparison with the sham control cohort. We used rectal temperature as a surrogate measure of core body temperature and thus the difference between initial and final measured temperatures with AMF exposure can indicate the extent of non-specific tissue heating [41,52,53]. Mean rectal temperature change for all cohorts is statistically insignificant when compared with sham controls, supporting the observation that the main source of total body (non-specific) heating is the water jacket, compensating for anaesthesia-induced hypothermia [37]. No statistically significant tumour heating was measured in the absence of nanoparticles. Conversely, significant tumour-specific heating is observed with combinations of AMF with BNF and BNF-lip formulations. The latter of these produces measurably greater tumour-associated heating than BNF-only mediated heating (Figure 6). The nature of this heating warrants further investigation.

Combined with the established X-ray opacity of ethiodised oil, the BNF-lip formulation may prove useful as a dual imaging marker of therapeutic tumour targeting. CT imaging may serve as the preferred imaging modality for assessing the pattern of BNF-lip intratumoural distribution, whereas MR imaging may serve for quantifying iron deposition.

Tumour growth delay studies were not investigated in this study, limiting the demonstration of therapeutic potential of this formulation in combination with chemotherapy, although the recently demonstrated enhancing effects of combining ionising radiation with BNF hyperthermia suggest a likely benefit. Toxicity and biodistribution studies were not performed to assess the accumulation of BNF-lip in other organs and potential effects on their function. Further study is needed to fully evaluate the pharmacological and therapeutic benefits to be gained by combining alternating magnetic field thermotherapy with intra-arterial chemotherapy.

Conclusion

The unique properties of a formulation of ethiodised oil and iron oxide nanoparticles comprising aggregated crystallite cores may serve as a novel platform for focal hyperthermia to treat liver cancer in an image-guided treatment paradigm. The BNF-lip formulation described in this work adopts the established clinical properties of ethiodised oil, leading to sustained intratumoural deposition of iron for at least 7 days following intra-arterial injection. These results are encouraging and motivate further research of the enhancement of the clinical procedure of chemoembolisation with magnetic nanoparticles.

Acknowledgments

The authors wish to thank Lauri Pipitone, Juls Blevins, Jorge Guzman and Theresa Caton for helping them with the animal handling and imaging.

References

1. Solomon SB, Silverman SG. Imaging in interventional oncology. Radiology. 2010; 257:624–40. [PubMed: 21084414]

2. Idée JM, Guiu B. Use of Lipiodol as a drug-delivery system for transcatheter arterial chemoembolization of hepatocellular carcinoma: a review. Crit Rev Oncol Hematol. 2013; 88:530–49. [PubMed: 23921081]

3. European Association for the Study of Liver, European Organization for Research and Treatment of Cancer. EASL-EORTC clinical practice guidelines: management of hepatocellular carcinoma. J Hepatol. 2012; 56:908–43. [PubMed: 22424438]

4. Kritzinger J, Klass D, Ho S, Lim H, Buczkowski A, Yoshida E, et al. Hepatic embolotherapy in interventional oncology: technology, techniques, and applications. Clin Radiol. 2013; 68:1–15. [PubMed: 22917735]

5. Lencioni R, Crocetti L. Local-regional treatment of hepatocellular carcinoma. Radiology. 2012; 262:43–58. [PubMed: 22190656]

6. Liapi E, Geschwind JF. Intra-arterial therapies for hepatocellular carcinoma: where do we stand? Ann Surg Oncol. 2010; 17:1234–46. [PubMed: 20405328]

7. Lewandowski RJ, Geschwind JF, Liapi E, Salem R. Transcatheter intraarterial therapies: rationale and overview. Radiology. 2011; 259:641–57. [PubMed: 21602502]

8. Liapi E, Georgiades CC, Hong K, Geschwind JF. Transcatheter arterial chemoembolization: current technique and future promise. Tech Vasc Interv Radiol. 2007; 10:2–11. [PubMed: 17980314]

9. Hildebrandt, B.; Gellermann, J.; Hanno, R.; Wust, P. Induced hyperthermia in the treatment of cancer. In: Minev, BR., editor. Cancer management in man: chemotherapy, biological therapy, hyperthermia and supporting measures, Cancer Growth and Progression. Vol. 13. Berlin: Springer; 2011. p. 365-77.

10. Ivkov R. Magnetic nanoparticle hyperthermia: a new frontier in biology and medicine? Int J Hyperthermia. 2013; 29:703–5. [PubMed: 24219798]

11. Kozissnik B, Bohorquez AC, Dobson J, Rinaldi C. Magnetic fluid hyperthermia: advances, challenges, and opportunity. Int J Hyperthermia. 2013; 29:706–14. [PubMed: 24106927]

12. Mitsumori M, Hiraoka M, Shibata T, Okuno Y, Masunaga S, Koishi M, et al. Development of intra-arterial hyperthermia using a dextran-magnetic complex. Int J Hyperthermia. 1994; 10:785–93. [PubMed: 7533813]

13. Mitsumori M, Hiraoka M, Shibata T, Okuno Y, Nagata Y, Nishimura Y, et al. Targeted hyperthermia using dextran magnetite complex: a new treatment modality for liver tumors. Hepatogastroenterology. 1996; 43:1431–7. [PubMed: 8975944]

14. Moroz P, Jones SK, Winter J, Gray BN. Targeting liver tumors with hyperthermia: Ferromagnetic embolization in a rabbit liver tumor model. J Surg Oncol. 2001; 78:22–9. [PubMed: 11519064]

15. Jones S, Winter J, Gray B. Treatment of experimental rabbit liver tumors by selectively targeted hyperthermia. Int J Hyperthermia. 2002; 18:117–28. [PubMed: 11911482]

16. Moroz P, Jones SK, Gray BN. The effect of tumor size on ferromagnetic embolization hyperthermia in a rabbit liver tumor model. Int J Hyperthermia. 2002; 18:129–40. [PubMed: 11911483]

17. Moroz P, Pardoe H, Jones SK, St Pierre TG, Song S, Gray BN. Arterial embolization hyperthermia: hepatic iron particle distribution and its potential determination by magnetic resonance imaging. Phys Med Biol. 2002; 47:1591–602. [PubMed: 12043822]

18. Sun H, Xu L, Fan T, Zhan H, Wang X, Zhou Y, et al. Targeted hyperthermia after selective embolization with ferromagnetic nanoparticles in a VX2 rabbit liver tumor model. Int J Nanomed. 2013; 8:3795–804.

19. Kumar CS, Mohammad F. Magnetic nanomaterials for hyperthermia-based therapy and controlled drug delivery. Adv Drug Deliv Rev. 2011; 63:789–808. [PubMed: 21447363]

20. Mouli SK, Tyler P, McDevitt JL, Eifler AC, Guo Y, Nicolai J, et al. Image-guided local delivery strategies enhance therapeutic nanoparticle uptake in solid tumors. ACS Nano. 2013; 7:7724–33. [PubMed: 23952712]

21. Gruettner C, Muller K, Teller J, Westphal F, Foreman AR, Ivkov R. Synthesis and antibody conjugation of magnetic nanoparticles with improved specific power absorption rates for alternating magnetic field cancer therapy. J Mag Magn Mat. 2007; 311:181–6.

22. Hedayati M, Attaluri A, Bordelon D, Goh R, Armour M, Zhou H, et al. New iron-oxide particles for magnetic nanoparticle hyperthermia: an in-vitro and in-vivo pilot study. Proc SPIE. 2013; 8584:041–10.
23. Wang L, Corum CA, Idiyatullin D, Garwood M, Zhao Q. T1 estimation for aqueous iron oxide nanoparticle suspensions using a variable flip angle SWIFT sequence. Magn Reson Med. 2013; 70:341–7. [PubMed: 23813886]
24. Dennis CL, Ivkov R. Physics of heat generation using magnetic nanoparticles for hyperthermia. Int J Hyperthermia. 2013; 29:715–29. [PubMed: 24131317]
25. Wabler M, Zhu W, Hedayati M, Attaluri A, Zhou H, Mihalic J, et al. Magnetic resonance imaging contrast of iron oxide nanoparticles developed for hyperthermia is dominated by iron content. Int J Hyperthermia. 2014; 30:192–200. [PubMed: 24773041]
26. Ivkov, R. Magnetic nanoscale particle compositions, and therapeutic methods related thereto. US Patent. 7,731,648.
27. Krycka KL, Jackson AJ, Borchers JA, Shih J, Briber R, Ivkov R, et al. Internal magnetic structure of dextran coated magnetite nanoparticles in solution using small angle neutron scattering with polarization analysis. J Appl Phys. 2011; 109:07B513.
28. Dennis CL, Krycka KL, Borchers JA, Desutels RD, van Lierop J, Huls NF, et al. Internal magnetic structure of nanoparticles dominates time-dependent relaxation processes in a magnetic field. Adv Func Mater. 2015; 25:4300–4311.
29. Branquinho LC, Carriao MS, Costa AS, Zufelato N, Sousa MH, Miotto R, et al. Effect of magnetic dipolar interactions on nanoparticle heating efficiency: implications for cancer hyperthermia. Sci Rep. 2013; 3:2887. [PubMed: 24096272]
30. Verde EL, Landi GT, Carriao MS, Drummond AL, Gomes JA, Vieira ED, et al. Field dependent transition to the non-linear regime in magnetic hyperthermia experiments: comparison between maghemite, copper, zinc, nickel and cobalt ferrite nanoparticles of similar sizes. AIP Advances. 2012; 2:032120.
31. Dennis CL, Jackson AJ, Borchers JA, Hoopes PJ, Strawbridge RR, Foreman AR, et al. Nearly complete regression of tumors via collective behavior of magnetic nanoparticles in hyperthermia. Nanotechnology. 2009; 20:395103. [PubMed: 19726837]
32. Dutz S, Kettering M, Hilger I, Müller R, Zeisberger M. Magnetic multicore nanoparticles for hyperthermia – influence of particle immobilization in tumor tissue on magnetic properties. Nanotechnology. 2011; 22:265102. [PubMed: 21576784]
33. Liapi E, Geschwind JF. Transcatheter arterial chemoembolization for liver cancer: is it time to distinguish conventional from drug-eluting chemoembolization? Cardiovasc Intervent Radiol. 2011; 34:37–49. [PubMed: 21069333]
34. Liapi E, Geschwind JF. Chemoembolization for primary and meta-static liver cancer. Cancer J. 2010; 16:156–62. [PubMed: 20404613]
35. De Baere T, Dufaux J, Roche A, Counnord JL, Berthault MF, Denys A, et al. Circulatory alterations induced by intra-arterial injection of iodized oil and emulsioins of iodized oil and doxorubicin: experimental study. Radiology. 1995; 194:165–70. [PubMed: 7997545]
36. Bordelon DE, Cornejo C, Gruttner C, Westphal F, DeWeese TL, Ivkov R. Magnetic nanoparticle heating efficiency reveals magneto-structural differences when characterized with wide ranging and high amplitude alternating magnetic fields. J Appl Phys. 2011; 109:124904.
37. Bordelon DE, Goldstein RC, Nemkov VS, Kumar A, Jackowski JK, DeWeese TL, et al. Modified solenoid coil that efficiently produces high amplitude AC magnetic fields with enhanced uniformity for biomedical applications. IEEE Trans Magn. 2012; 48:47–52. [PubMed: 25392562]
38. Attaluri A, Nusbaum C, Wabler M, Ivkov R. Calibration of a quasi-adiabatic magneto-thermal calorimeter used to characterize magnetic nanoparticle heating. J Nanotechnol Eng Med. 2013; 4:011006.1–8.
39. Kumar A, Attaluri A, Mallipudi R, Cornejo C, Bordelon D, Armour M, et al. Method to reduce non-specific heating of small animals in solenoid coils. Int J Hyperthermia. 2013; 29:106–20. [PubMed: 23402327]

40. Hedayati M, Thomas O, Abubaker-Sharif B, Zhou H, Cornejo C, Zhang Y, et al. The effect of cell-cluster size on intracellular nanoparticle-mediated hyperthermia: is it possible to treat microscopic tumors? Nanomedicine. 2013; 8:29–41. [PubMed: 23173694]
41. Attaluri A, Kandala SK, Zhou H, Cornejo C, Armour M, Hedayati M, et al. Magnetic nanoparticle hyperthermia enhances radiation therapy: a study in mouse models of human prostate cancer. Int J Hyperthermia. 2015; 31:359–74. [PubMed: 25811736]
42. Institute for Laboratory Animal Research. Guide for the care and use of laboratory animals. 7. Washington, DC: National Academies Press; 1996.
43. Lee KH, Liapi E, Buijs M, Vossen J, Hong K, Georgiades C, et al. Considerations for implantation site of VX2 carcinoma into rabbit liver. J Vasc Interv Radiol. 2009; 20:113–17. [PubMed: 19028118]
44. Lee KH, Liapi E, Buijs M, Vossen JA, Prieto-Ventura V, Syed LH, et al. Percutaneous US-guided implantation of VX-2 carcinoma into rabbit liver: a comparison with open surgical method. J Surg Res. 2009; 155:94–9. [PubMed: 19181344]
45. Lee KH, Liapi E, Ventura VP, Buijs M, Vossen JA, Vali M, et al. Evaluation of different calibrated spherical polyvinyl alcohol microspheres in transcatheter arterial chemoembolization: VX2 tumor model in rabbit liver. J Vasc Interv Radiol. 2008; 19:1065–9. [PubMed: 18589321]
46. Lee KH, Liapi E, Vossen JA, Buijs M, Ventura VP, Georgiades C, et al. Distribution of iron oxide-containing Embosphere particles after transcatheter arterial embolization in an animal model of liver cancer: evaluation with MR imaging and implication for therapy. J Vasc Interv Radiol. 2008; 19:1490–6. [PubMed: 18755602]
47. Lee KH, Liapi EA, Cornell C, Reb P, Buijs M, Vossen JA, et al. Doxorubicin-loaded QuadraSphere microspheres: plasma pharmacokinetics and intratumoral drug concentration in an animal model of liver cancer. Cardiovasc Intervent Radiol. 2010; 33:576–82. [PubMed: 20087738]
48. Luo TY1, Shih YH, Chen CY, Tang IC, Wu YL, Kung HC, et al. Evaluating the potential of (188)Re-ECD/lipiodol as a therapeutic radiopharmaceutical by intratumoral injection for hepatoma treatment. Cancer Biother Radiopharm. 2009; 24:535–41. [PubMed: 19877883]
49. Solorio L, Patel RB, Wu H, Krupka T, Exner AA. Advances in image-guided intratumoral drug delivery techniques. Ther Deliv. 2010; 1:307–22. [PubMed: 22816134]
50. Wang Y-XJ, Hussain SM, Krestin GP. Superparamagnetic iron oxide contrast agents: physicochemical characteristics and applications in MR imaging. Eur Radiol. 2001; 11:2319–31. [PubMed: 11702180]
51. Teeguarden JG, Hinderliter PM, Orr G, Thrall BD, Pounds JG. Particokinetics in vitro: dosimetry considerations for in vitro nanoparticle toxicity assessments. Toxicol Sci. 2007; 95:300–12. [PubMed: 17098817]
52. Ivkov R, DeNardo SJ, Daum W, Foreman A, Goldstein R, DeNardo GL. Application of high amplitude alternating magnetic fields for heat induction of nanoparticles localized in cancer. Clin Cancer Res. 2005; 11:S7093–S103.
53. Trakic A, Liu F, Crozier S. Transient temperature rise in a mouse due to low-frequency regional hyperthermia. Phys Med Biol. 2006; 51:1673–91. [PubMed: 16552097]

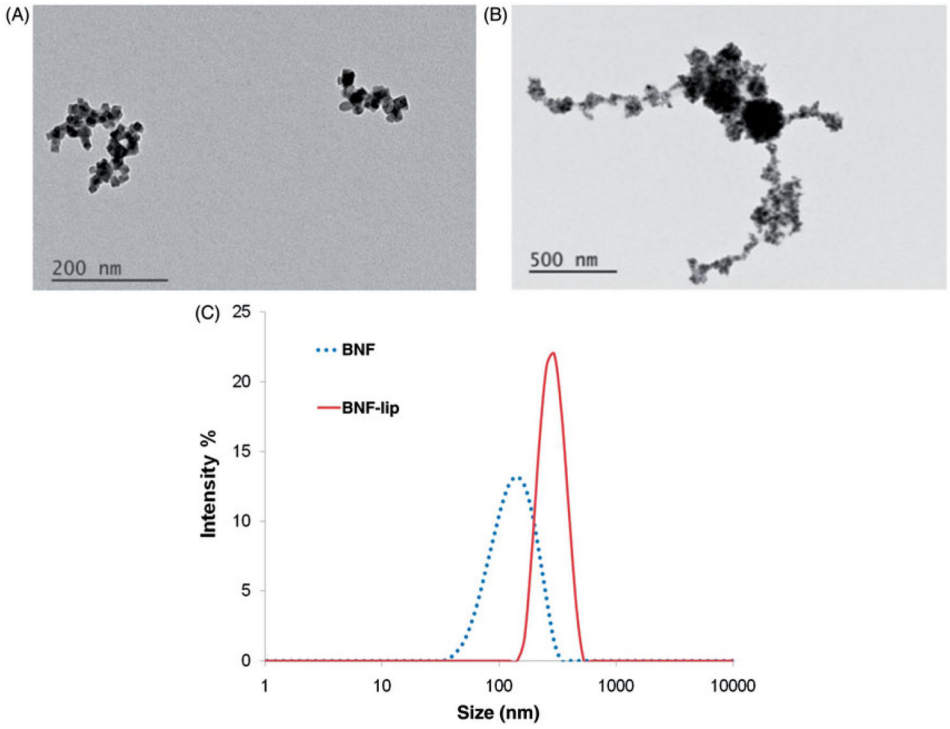

Figure 1.

BNF particle size characterisation in aqueous suspensions and as BNF-lip. (A) TEM images of BNF in aqueous suspension, and (B) cBNF-lip; (C) z-averaged values of intensity obtained from photon correlation spectroscopy (PCS). Note: images have different magnifications.

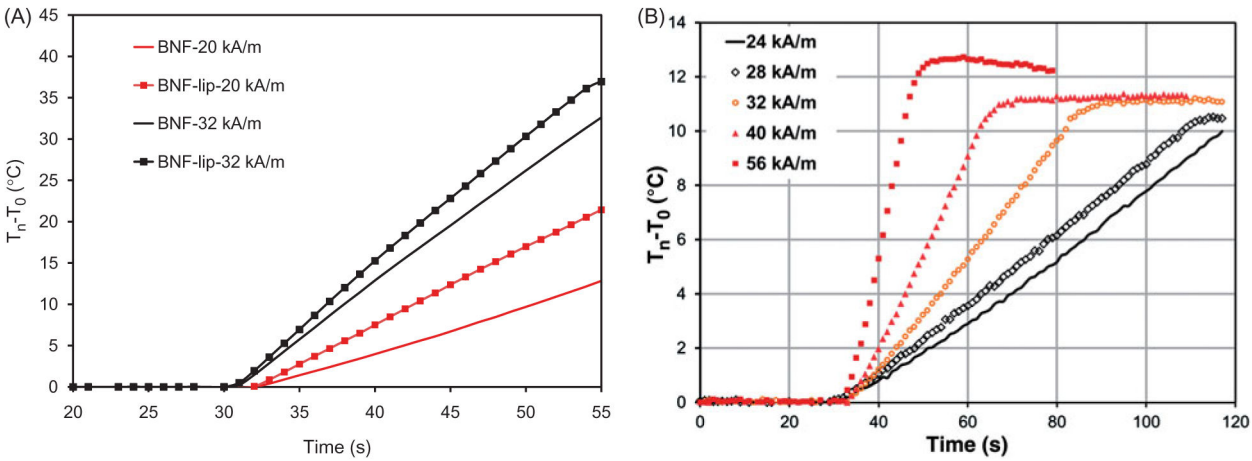

Figure 2.

BNF versus BNF-lip formulation heating when exposed to AMF. (A) Direct comparison of specific heating rate of BNF with BNF-lip, (dT/dt) × (1/mg Fe), measured by estimating the slope of temperature versus time curve, where dT/dt is the slope of temperature versus time curve determined using methods reported by Bordelon et al. [36]. Heating comparisons were performed at peak amplitudes 20 and 32 kA/m and 155 (± 5) kHz. (B) Specific heating rate measurements of BNF-lip formulation with varying amplitude at 155 (± 5) kHz.

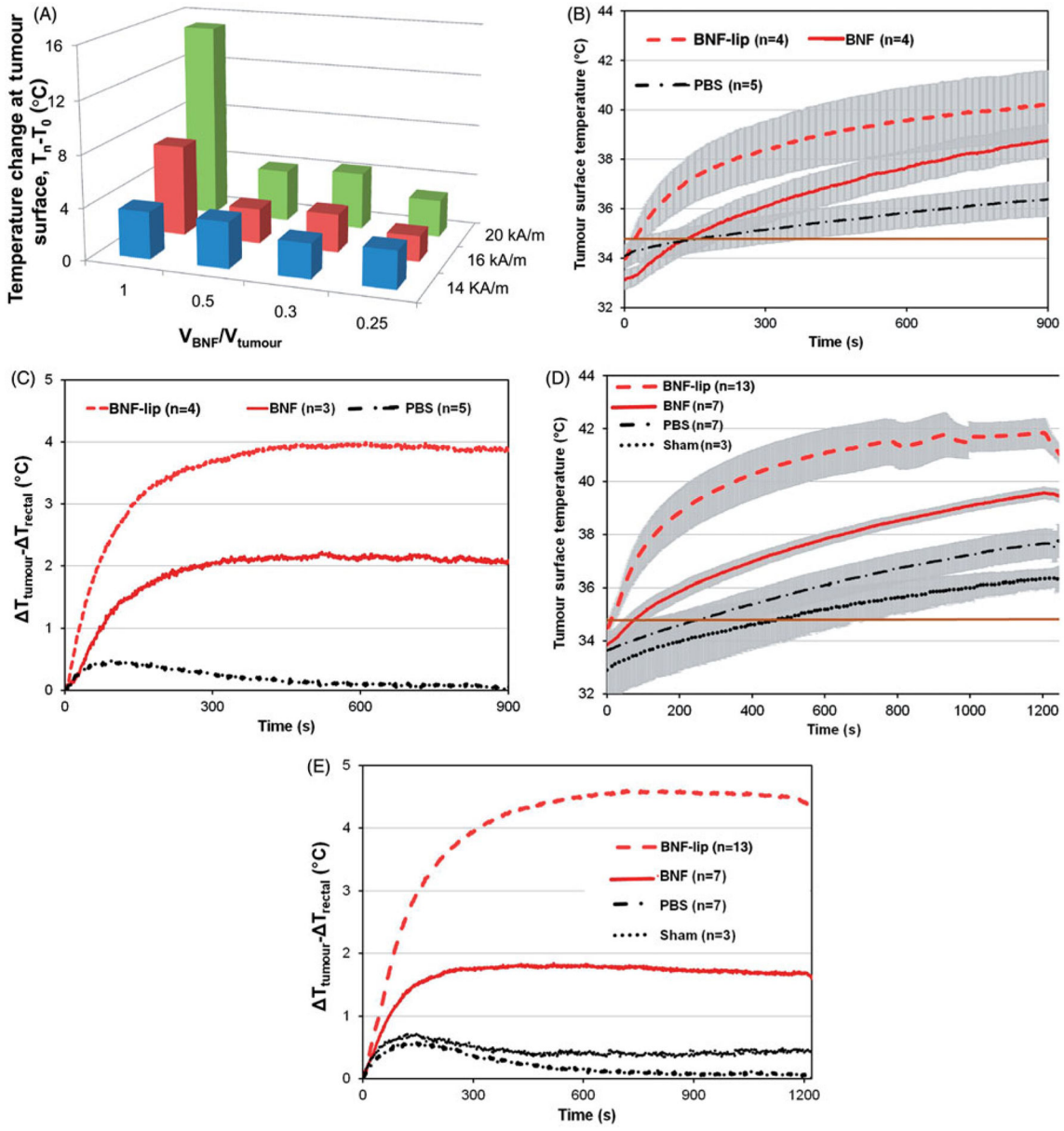

Figure 3.

(A) Measured temperature change (final – initial) at the surface of HepG2 tumours following heating in AMF for group I mice (1 per cohort; see text). Tumours were injected with BNF-lip formulation at varying dose combinations (V_{BNF}/V_{tumour}) and exposed to AMF with variable amplitude. Abscissa represents the injected dose, measured as the ratio of injected volume BNF suspension and measured tumour volume. Treatment duration was 15 min. (B) Mean values of tumour surface temperature plotted with time comparing heating in HepG2 tumours in group II mice following intratumoural injections of one of PBS, BNF, or BNF-lip. AMF amplitude was fixed at 20 kA/m and duration of exposure was 15 min. Treatments commenced 18 h after intratumoural injections (D =0.5 V_{tumour} (mL)). (C) Mean time–temperature data comparing difference of tumour surface temperature with rectal

temperatures for the cohort of mice described in B. (D) As in B; however, duration of treatment was 20 min and subject group included additional sham (AMF 0 kA/m) cohort. (E) Mean tumour–rectal temperature differences obtained from cohort described in D. Grey shading in Figures 3B and 3D are created by error bars representing the calculated standard error of mean values.

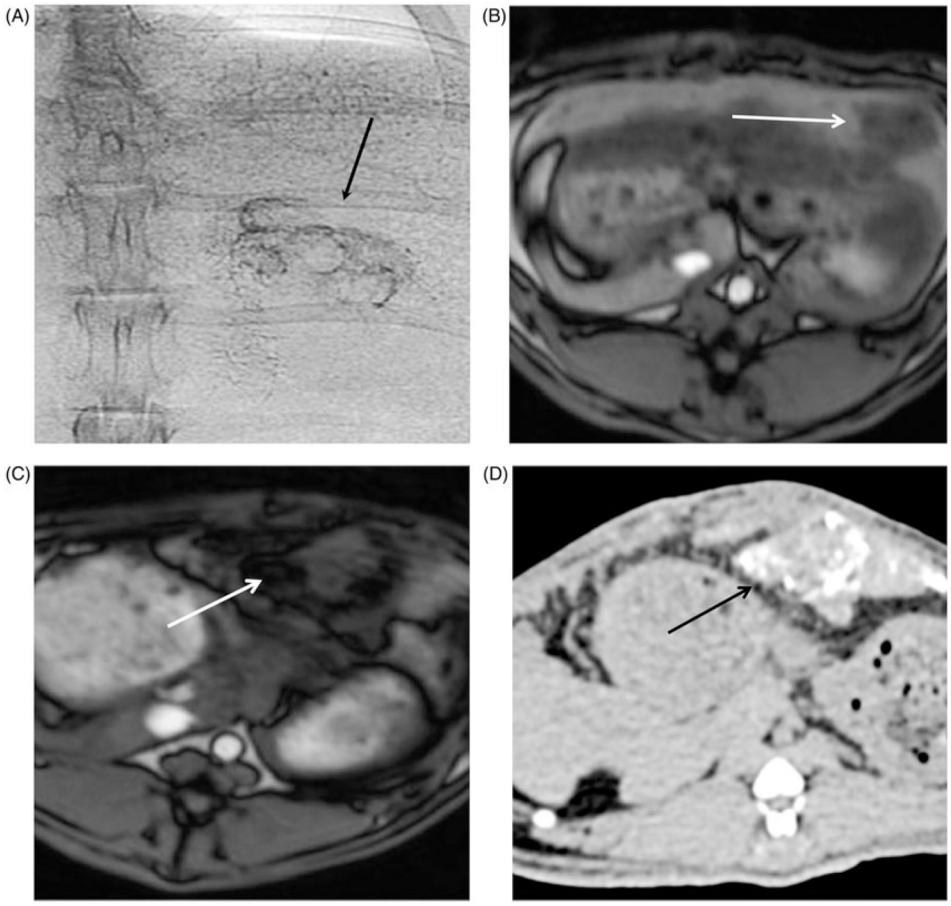

Figure 4.

Representative X-ray (CT) and magnetic resonance (MR) images of rabbit liver and VX2 tumours. (A) Single-shot image of rabbit abdominal region during angiography injection of BNF-lip. (B) Axial T1 image of liver VX2 tumour in a rabbit before intra-arterial injection of BNF-lip formulation. (C) Axial T1 image of liver VX2 tumour in a rabbit at 7 days after intra-arterial BNF-lip injection. Note the pronounced paramagnetic feature of iron at the tumour site. (D) X-ray (CT) axial unenhanced image of the liver and VX2 tumour at 7 days after intra-arterial BNF-lip injection. Note the intratumoural deposition of BNF-lip (positive X-ray material in the tumour area). The arrow on each image indicates the location of the tumour.

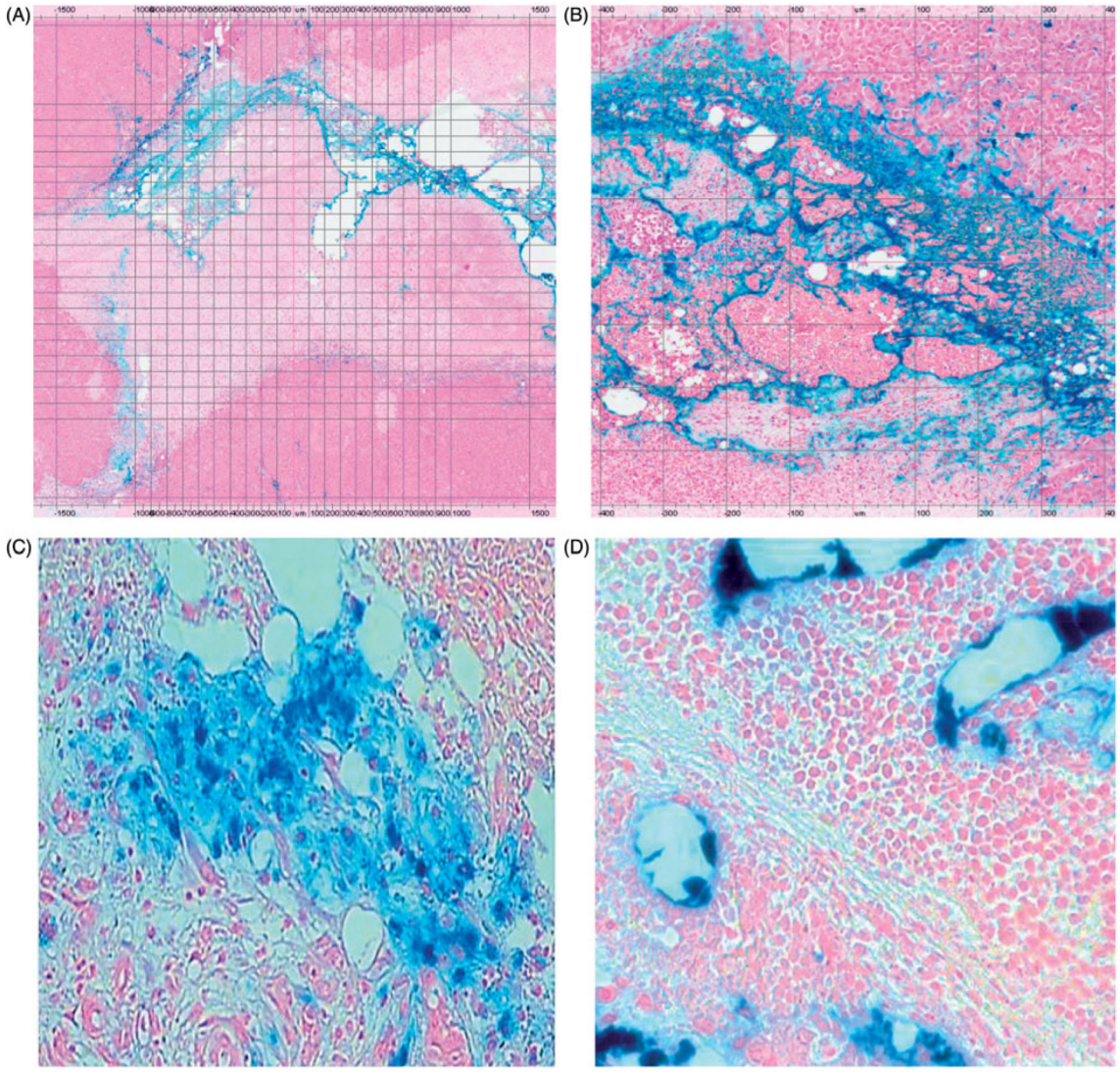

Figure 5.

Histopathological images of Prussian blue-stained tissues. (A) Section of HepG2 tumour (2× magnification) harvested 3 days post-AMF–hyperthermia with BNF-lip showing necrotic cells in immediate vicinity of tumour evidenced by pale colouring, and localisation of BNF particles (blue) in the vicinity of the presumed needle track. (B) As in A, but at 8× magnification. (C) Section of liver VX2 tumour harvested at 7 days after intra-arterial injection with BNF-lip. Note that iron is deposited either in the tumour interstitium (C) and/or inside the tumour vessels (D).

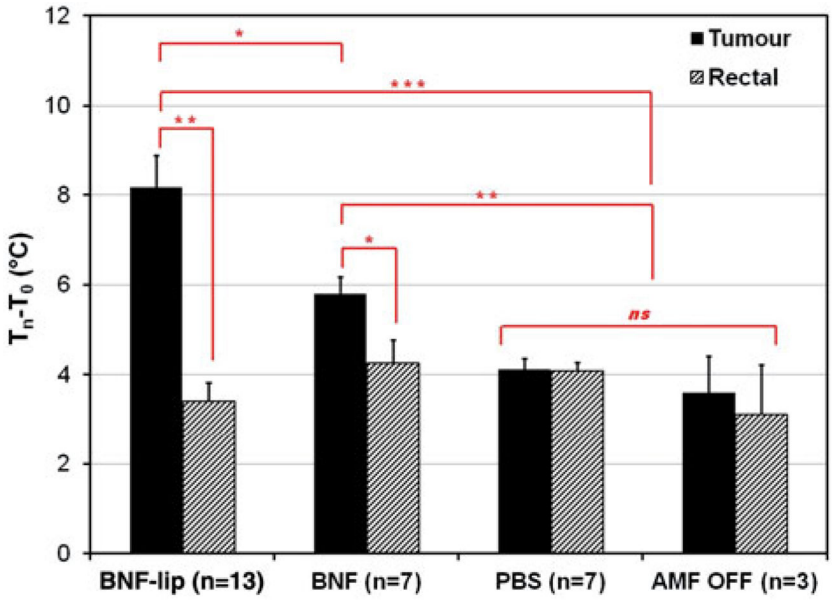

Figure 6.

Mean tumour and rectal temperature changes (final – initial) measured for cohorts of mice injected with one of (D =0.5V_{tumour} (ml)), PBS (saline control), BNF, or BNF-lip exposed to AMF 18 h after injection to AMF at 20 kA/m for duration of 20 min. Sham controls were injected with either PBS or BNF and placed in the AMF coil (as with the other cohorts) for 20 min with 0 kA/m amplitude. *p <0.05; **p <0.01; ***p <0.001; *ns,* not significant, p >0.05.

Table 1

Summary of treatment parameters and measured HepG2 tumour temperatures in mice exposed to AMF.

						T_0 (°C)		T_{max} (°C)		ΔT (°C)	
Mouse code	**Injected material**	**Tumour volume (cm^3)**	**Injected volume (mL)**	**H (kA/m)**	**Treatment time (min)**	**Tumour**	**Rectal**	**Tumour**	**Rectal**	**Tumour**	**Rectal**
1. 3-LF (PBS)	PBS	0.115	0.058	16	15	34.6	33.4	37.54	36.5	2.94	3.13
2. 2-RR (BNF)	BNF	0.183	0.092	16	15	35.07	33.5	38.31	37.72	3.24	4.18
3. 3-RR (BNF)	BNF	0.112	0.056	16	15	35.26	33.2	40.81	37.24	5.55	4.08
4. 2-RF (BNF)	BNF	0.114	0.057	16	15	32.78	31.8	33.91	32.69	1.13	0.93
5. 1-LF (PBS)	PBS	0.111	0.056	20	15	33.9	32.1	36.57	35.45	2.67	3.38
6. 1-RR (PBS)	PBS	0.114	0.057	20	15	33.51	31.4	36.53	34.5	3.02	3.09
7. 2-LF (PBS)	PBS	0.114	0.057	20	15	32.78	31.8	33.91	32.69	1.13	0.93
8. 2-LR (PBS)	PBS	0.125	0.063	20	15	35.08	33.4	37.5	36.01	2.42	2.6
9. 4-UM(PBS)	PBS	0.193	0.097	20	15	35.13	34.3	37.77	36.4	2.64	2.13
10. 1-LR (BNF)	BNF	0.129	0.066	20	15	32.43	31.6	37.79	35.32	5.36	3.73
11. 1-RF (BNF)	BNF	0.106	0.053	20	15	30.41	31.5	40.31	32.89	9.9	1.35
12. 4-RF(BNF)	BNF	0.132	0.066	20	15	33.06	32.1	38.51	36.14	5.45	4.05
13. 6-LR(BNF)	BNF	0.244	0.122	20	15	33.91	33.4	40.34	37.62	6.43	4.25
14. 2-UM (BNF/LIP)	BNF/Lip	0.11	0.055	20	15	34.75	33.6	41.62	36.24	6.87	2.61
15. 3-LR (BNF/LIP)	BNF/Lip	0.104	0.052	20	15	33.63	30.8	43.32	35.38	9.69	4.63
16. 3-UM (BNF/LIP)	BNF/Lip	0.133	0.067	20	15	33.43	33	37.25	33.93	3.82	0.91
17. 6-RR(BNF/Lip)	BNF/Lip	0.184	0.092	20	15	34.13	33.1	38.92	35.45	4.79	2.33
18. 1-UM (BNF/LIP)	BNF/Lip	0.156	0.078	24	15	33.39	31.5	46.74	36.5	13.35	5.01
19. 10-LR (BNF)	BNF	0.147	0.07	0	20	33.57	33	36.56	35.86	2.99	2.82
20. 10-LR (BNF)	BNF	0.136	0.07	0	20	34.5	34.7	37.12	36.1	2.62	1.38
21. 12-LR (PBS)**	PBS	0.226	0.11	0	20	30.63	30	35.83	35.11	5.2	5.15
22. 5-LF (PBS)	PBS	0.159	0.08	20	20	33.01	31.1	36.29	34.41	3.28	3.28
23. 6-LF (PBS)	PBS	0.129	0.065	20	20	32.83	31.2	37.26	35.57	4.43	4.33
24. 8-RF (PBS)	PBS	0.099	0.05	20	20	34.86	32.4	38.51	35.93	3.65	3.56
25. 7-LR (PBS)	PBS	0.099	0.05	20	20	35.93	32.3	40.35	36.55	4.42	4.21
26. 7-UM (PBS)	PBS	0.124	0.06	20	20	33.71	31	38.45	35.53	4.74	4.52
27. 9-LF (PBS)	PBS	0.125	0.06	20	20	31.91	31	36.82	35.63	4.91	4.65

						T_0 (°C)		T_{max} (°C)		ΔT (°C)	
Mouse code	**Injected material**	**Tumour volume (cm^3)**	**Injected volume (mL)**	**H (kA/m)**	**Treatment time (min)**	**Tumour**	**Rectal**	**Tumour**	**Rectal**	**Tumour**	**Rectal**
28. 11-LF (PBS)	PBS	0.122	0.06	20	20	33.22	32.2	36.57	36.24	3.35	4.03
29. 5-UM (BNF)	BNF	0.112	0.056	20	20	34.23	33.2	39.18	36.19	4.95	3.02
30. 4-LR (BNF)	BNF	0.152	0.076	20	20	34.94	31.5	40.57	36.42	5.63	4.96
31. 9-LR (BNF)	BNF	0.134	0.07	20	20	35.24	33.1	39.63	35.53	4.39	2.46
32. 7-RF (BNF)	BNF	0.116	0.06	20	20	33.59	32.4	39.15	37.45	5.56	5.1
33. 12-RR (BNF)	BNF	0.14	0.07	20	20	33.41	32.5	40.21	36.67	6.8	4.19
34. 13-LR (BNF)	BNF	0.126	0.06	20	20	33.17	32.8	38.99	36.4	5.82	3.56
35. 12-RF (BNF)	BNF	0.132	0.07	20	20	32.26	31.3	39.67	37.78	7.41	6.51
36. 6-RF (BNF/Lip)	BNF/Lip	0.113	0.057	20	20	33.39	33.2	46.92	36.06	13.53	2.91
37. 9-UM (BNF/Lip)	BNF/Lip	0.209	0.105	20	20	34.12	32.2	42.83	34.65	8.71	2.5
38. 8-LR (BNF/Lip)	BNF/Lip	0.113	0.06	20	20	34.79	32.2	42.23	37.19	7.44	4.98
39. 9-RR (BNF/Lip)	BNF/Lip	0.141	0.07	20	20	35.55	32.7	39.64	36.36	4.09	3.63
40. 7-RR (BNF/Lip)	BNF/Lip	0.1	0.05	20	20	35.6	34.1	43.31	35.89	7.71	1.77
41. 8-RR (BNF/Lip)	BNF/Lip	0.106	0.05	20	20	33.7	32.4	41.96	37.92	8.26	5.56
42. 11-UM (BNF/Lip)	BNF/Lip	0.114	0.06	20	20	32.64	31.5	40.06	36.35	7.42	4.88
43. 13-RF (BNF/Lip)	BNF/Lip	0.159	0.08	20	20	33.18	32.3	42.19	37.04	9.01	4.73
44. 10-UM (BNF/Lip)	BNF/Lip	0.121	0.06	20	20	34.21	32.2	41.09	37.22	6.88	5.02
45. 12-UM (BNF/Lip)	BNF/Lip	0.113	0.06	20	20	34.75	33.8	39.85	36.5	5.1	2.73
46. 5-RR(BNF/Lip)	BNF/Lip	0.126	0.063	20	20	34.66	34.7	43.33	36.2	8.67	1.5
47. 6-UM(BNF/Lip)	BNF/Lip	0.155	0.078	20	20	36.63	35.7	49.59	37.83	12.96	2.14
48. 7-LF(BNF/Lip)	BNF/Lip	0.123	0.06	20	20	35.34	33.7	41.7	35.77	6.36	2.07

H, denotes peak field amplitude;

T_0 denotes measured temperature at time = 0 min (i.e. initial temperature);

T_{max} denotes maximum measured temperature;

‘delta’T denotes differece of maximum and initial temperature.